Improving the accuracy in particle concentration measurements of a balloon-borne optical particle counter UCASS

Sina Jost[1], Ralf Weigel[1], Konrad Kandler[2], Luis Valero[2], Jessica Girdwood[3, 4], Chris Stopford[3], Warren Stanley[3], Luca K. Eichhorn[1], Christian von Glahn[1], and Holger Tost[1]

[1]Institute for Physics of the Atmosphere, Johannes Gutenberg University, Mainz, Germany

[2]Institute for Applied Geosciences, Technical University Darmstadt, Germany

[3]Particle Instruments & Diagnostics Research Group, University of Hertfordshire, Hatfield, Hertfordshire, AL10 9AB, United Kingdom

[4]National Centre for Atmospheric Science, School of Earth, Atmospheric and Environmental Sciences, University of Manchester, Manchester, M13 9PL, United Kingdom

Corresponding authors: Sina Jost (sjost@students.uni-mainz.de) and Ralf Weigel, (weigelr@uni-mainz.de)

1 Abstract

For balloon-borne detection of aerosols and cloud droplets (diameter $0.4 < D_p < 40$ µm), a passive-flow Universal Cloud and Aerosol Sounding System (UCASS) was used, whose sample flow rate is conventionally derived from balloon ascent rates using GPS or pressure measurements. Improvements are achieved by implementing thermal flow sensors (TFS) 94 mm downstream of the UCASS detection region for continuously measuring true UCASS sample flow velocities. UCASS-mounted TFS were calibrated during wind tunnel experiments at up to 10 m s^{-1} also under various angles-of-attack (AOA), as these vary during actual balloon ascents. It was found that the TFS-calibration is determined with sufficient precision using three calibration points at tunnel flows of $\sim$ 2, 5, and 8 m s^{-1}, simplifying efficient TFS-upgrades of numerous UCASS. In iso-axial alignment, UCASS flows are accelerated (by $\sim$ 11.3 %) compared to tunnel flows (at 2 – 8 m s^{-1}). In-flight comparisons up to 7.5 km height revealed that UCASS sample flows rarely match the balloon's ascent rate. Laboratory experiments show that equality ($v_{GPS} = v_{TFS}$) is achieved only at AOA $\neq 0°$, potentially affecting the UCASS-internal flow pattern and particle transmission efficiency in flight. To minimise errors on calculated UCASS-based particle number concentrations, real-time measurements of the true UCASS flow velocity are recommended.

2 Introduction

Weather balloon soundings are an established method to carry out in-situ measurements up to high altitudes in the atmosphere (e.g. Golden et al. (1986), Vömel and Fujiwara (2021), or Vömel and Ingleby (2023)). Balloons filled with helium or hydrogen can reach heights of up to 40 km. Due to a moderately variable ascent rate of $\sim$ 5 - 6 m s^{-1} on average, the troposphere and stratosphere are probed with a higher vertical resolution compared to aircraft measurement due to the higher climb and descent rates of the latter (at least 6 m s^{-1} and usually more, cf. Eufar (2000)). In conventional operation, a radiosonde is used as payload deployed on a thin cord of about 50-60 m length below the ascending weather balloon. Radiosondes are used to directly measure atmospheric pressure, humidity, temperature, and wind parameters during the ascent, while the data are sent in real time via radio to the receiving station (see, e.g., Dirksen et al. (2020)).

Balloon-based vertical soundings with radiosondes allow for characterising the current state of the atmosphere, from which atmospheric properties such as stability or stratification can be derived. The payload of the weather balloon can be extended beyond the sole use of radiosondes, for example by including an ozone probe (cf. Smit et al. (2024) and references therein) and/or optical particle counters (Matsumura et al. (2001); Kasai et al. (2003); Smith et al. (2019); Kezoudi et al. (2021); Snels et al. (2021)). Both ozone, as an atmospheric trace gas, as well as aerosols and clouds have a major influence on the Earth system. Aerosols and clouds influence the Earth's energy balance (by absorbing and scattering short-wave radiation), the global water cycle (through the formation of precipitation) and the atmospheric dynamics (through the conversion of latent heat in the phase transitions of water). Considering, that aerosols and cloud droplets modify radiative fluxes (see, e.g., Stier et al. (2024) or Ipcc (2023)), a better understanding of their size, number and vertical distribution is required and the vertical distribution of aerosols and cloud droplets need to be frequently investigated. The University of Hertfordshire (UK) has developed an optical particle spectrometer for balloon soundings: The "Universal Cloud and Aerosol Sounding System" (UCASS, see Smith et al. (2019); Kezoudi et al. (2021); Girdwood et al. (2022); Girdwood (2023), Schön et al. (2024)) is used to detect aerosol particles and cloud droplets with diameters of 0.4 to 40 μm. The probe's measuring principle is described in detail in Sect. 3.

In general, the thought model underlies the balloon sounding, that the horizontal wind that drifts the balloon or influences its geographical position has almost no or a negligible influence in the inertial system of the balloon itself, unless gusty winds or strong wind shear prevail. Hence, regarding the horizontal wind component, there is almost no relative horizontal wind aboard the balloon or its payload. The predominant flow relative to the balloon and its payload that mainly drives the air flow through a UCASS is the vertical wind component, which in our case is determined by the balloon's lift, i.e. its ascent rate.

To calculate a particle number concentration from the particle number detected (per unit time) by a balloon-borne UCASS, the sample volume flow rate through the UCASS detection region must be known. Conventionally, the sample volume flow was determined using balloon ascent rates (Kezoudi et al., 2021) derived from GPS or pressure measurements. This approach has two major disadvantages: a) a zero horizontal wind velocity is inherently assumed, and b) changes in airflow caused by the instrument housing, or small fluctuations remain unconsidered. One goal of this work therefore is to modify a UCASS such that a thermal flow sensor (TFS) is used to continuously determine the flow rates through a balloon-borne UCASS. This enables the accurate and precise

76   determination of particle concentrations (and inferred microphysical quantities) at a higher
77   confidence level. Beyond that, this study is a prerequisite for investigations based on UCASS
78   measurements during our balloon missions in Central Europe during summer of the years 2023
79   and 2024. Ultimately, the proposed improvements may provide support for UCASS applications
80   by other users.

81   The present publication is structured as follows. First, the instrument is described. This is
82   followed by reports on the testing and characterization of the method of mechanically coupling
83   the TFS to the UCASS (Sect. 3.5.1). Subsequently, the experiments aiming at the optimum position
84   of the TFS within the flow through a UCASS are described (Sect. 3.5.2). The TFS are then calibrated
85   against a reference flow sensor (Prandtl pitot tube, PPt) within the flow through a UCASS (Sect.
86   3.5.3). Based on a numerical simulation, it has already been assumed that the flow velocity within
87   the iso-axially aligned UCASS would increase by 12 % as compared to the ambient air flow speed
88   of 5 m s^{-1} (Smith et al., 2019). Therefore, in this work the PPt-measured ambient flow velocities
89   and TFS-detected flow velocity inside the UCASS are compared (Sect. 4.2). The impact of a non iso-
90   axial alignment (i.e. when the angle of attack, AOA, towards the UCASS varies due to the balloon-
91   payload's pendulum motion) on the flow velocities through the UCASS and on the TFS calibration
92   curves are investigated (Sect. 4.3 and 4.4). Finally, balloon soundings with the UCASS - TFS
93   combination are used to prove the TFS performance under atmospheric conditions (Sect. 5). The
94   findings are summarised in the conclusion section.

95   3 Instruments and methods

96   3.1 Universal Cloud and Aerosol Sounding System (UCASS)

97   The UCASS is an optical particle spectrometer (nominal detection range $0.4 < D_p < 40$ μm; Smith et
98   al. (2019), Girdwood (2023)). Due to its small size, low weight and comparatively low cost
99   (approx. 2700 € per unit), the UCASS is well suitable for balloon soundings. The UCASS is of
100   tubular shape with 183 mm in length and with an outer diameter of 64 mm at a weight of about
101   280 g. A hollow flow tube with quasi-elliptical cross-section of 40 mm × 30 mm diameter extends
102   along the longitudinal axis of the UCASS, through which the sample air flows and in which the
103   particles are detected. Particle detection with UCASS is carried out by optical detection of the
104   scattered light caused by particles upon crossing a diode-emitted laser beam. The optical system
105   of the UCASS defines a particle detection region of 0.5 mm^2 in size (Girdwood, 2023). In Fig. 1, the
106   principal setup of the UCASS instrument is illustrated, for more details see Smith et al. (2019),
107   Girdwood et al. (2022), or Girdwood (2023).

108   Particles are counted, which pass through the instrument's optically sensitive region along the
109   detection laser. The ratio of the scattered light generated by a penetrating particle is determined
110   by means of two annular elements in the detector optics. This signal ratio is judged according to
111   whether a detection event contributes an accepted count value or not. Based on scattered light
112   intensity, the accepted counts are categorised into size classes (16 bins) using size-based look-up
113   tables obtained by calibrations and based on Mie theory. Depending on the chemical composition
114   of detected particles, different refractive indices must be considered, for example between 1.31+0j
115   (water) and 1.52+0.002j (Saharan dust) (see Girdwood (2023) for further, more specific details)
116   whilst for Saharan dust also other values are found, e.g. 1.53−0.0015j (Kandler et al., 2007).
117   Knowledge of the flow velocity and the dimensions of the sensing volume is required to
118   determining accurate particle concentrations.

3.2 The thermal flow sensor (TFS)

The thermal flow sensor (TFS) model "FLW-122" for the gaseous media by B+B Thermo-Technik GmbH was used for this study. The TFS has a length of 6.9 mm, is 2.4 mm wide, and 0.2 mm high (without electrical connections). The TFS surface consists of two platinum resistor elements, one of which is the heater and the other is the reference element. The heater is a small-sized low-resistance element ($R_H(0\ °C) = 45\ \Omega$), the reference element ($R_S(0\ °C) = 1200\ \Omega$) is of high electrical resistance. The two platinum resistors are interconnected and are adjusted via applied voltage to a specified temperature difference. The heat dissipation from the heater to the environment corresponds to the energy loss per unit of time, which in turn corresponds to the power P converted in the resistor.

The temperature of the heating resistor decreases with increasing rate of flow surrounding the TFS. As platinum is a PTC thermistor, the conductivity of the resistor increases as the temperature falls, hence the resistance of the heater decreases. To counteract this and to maintain the differential temperature between heater and reference, the voltage is increased. The higher the flow velocity, the higher is the voltage (hereafter: signal voltage) required to maintain the temperature difference. According to the sensor data sheet (B+B-Thermo-Technik, 2016), the sensor's response sensitivity is 0.01 m s^{-1} with an accuracy of better than 3 % and a temperature sensitivity of usually less than 0.1 % K^{-1}. The raw TFS data is recorded with a resolution of at least 4 Hz and then averaged to the common 1 Hz data basis. Thus, most important variabilities in the UCASS-internal flow should be captured in sufficient resolution. In addition, low-frequency influences such as the pendulum motion (order of magnitude 0.1 Hz) and the rotation (of 1 Hz at most) of the balloon payload are also temporally resolved. Further detailed information on the TFS (e.g. concerning power and sensitivity of the implemented Z-diode) may be found in the manufacturer's manual (B+B-Thermo-Technik, 2016).

For TFS calibrations, the following parameterisation, a modified form of King's law (Guellouz and Tavoularis, 1995), is often used:

$$U^2 = A + B \cdot v_{TFS}^N\,, \qquad\qquad 1$$

where A (in V^2), B (in V^2 s m^{-1}), and N (dimensionless) are coefficients determined by calibrations, v_{TFS} is the flow velocity (in m s^{-1}) and U is the electrical output voltage (V). Rearrangement of Eq. 1 leads to the desired expression for the flow velocity (here v_{TFS}) as a function of measured voltage. King's law, a combination of Nusselt number and Reynolds number (see Cardell (1993) or Bearman (1971)), is primarily influenced by temperature fluctuations due to the temperature dependence of air's thermal conductivity and the dependence of the kinematic viscosity on the air density. Extensions of this equation by correction terms allow for considering changes of ambient temperature (see Cimbala and Park (1990)). On the one hand, these corrections apply to significantly warmer temperatures (300 – 307 K) than relevant for balloon soundings, and on the other hand require a set of temperature measurements, including the accurate temperature of the TFS surface itself. The TFS calibrations to assign a flow velocity to the output signal were carried out under laboratory conditions. To account for the dependence of the in-flight flow measurement on air density, a corresponding correction (dependent on static air pressures and ambient temperatures upon vertical sounding) is applied to measured data during post-flight analyses.

Based on the ideal gas law and on laboratory conditions during calibrations (p_0, T_0, and humidity expressed as virtual temperature), the correction v_{TFS}^{corr} is obtained by multiplying v_{TFS} (according to Eq. 1) with a correction factor (at given ambient conditions p_{amb}, T_{amb}):

163
$$v_{\text{TFS}}^{\text{corr}} = v_{\text{TFS}} \frac{p_0}{p_{\text{amb}}} \cdot \frac{T_{\text{vi}}}{T_0}$$

164 The virtual temperature T_{vi} was used instead of the ambient temperature T_{amb}. Hence, any change
165 in air's molar weight, air's mass density, and heat capacity due to water vapor load is accounted
166 for. As long as no phase conversion occurs the temperature ratio also reflects the current moisture
167 conditions in the atmosphere.

168 In addition, a cold chamber test was carried out at various temperatures down to – 20°C
169 (electronic supplement, S1) to investigate the sensitivity of the TFS system (particularly its
170 electronic compounds) to significantly colder temperatures than those under laboratory
171 conditions.

172 To mount the TFS on the UCASS, a 3D-printed polylactide case was produced. This was precisely
173 adapted to the dimensions of the inner flow tube and the outer shape of the UCASS and extends
174 the total length of the UCASS by a further 49 mm (cf. Fig. 2).

3.3 The Prandtl-Pitot tube
175
176 The Prandtl-Pitot tube (PPt) model "TSI 8710 plus" (re-calibrated in July 2022 for flow velocities
177 of 1 – 10 m s^{-1}) by TSI Inc. was used as reference instrument for calibrating the TFS. Via the pitot
178 tube's entry, aligned against the direction of flow, the stagnation pressure (the sum of the dynamic
179 and static pressure components) is measured. The outer tube of the Prandtl-instrument with ring-
180 shaped perforation, allows for measuring the static pressure component. Conversion of
181 Bernoulli's theorem to resolve to the flow velocity, leads to:

182
$$v_{\text{PPt}} = \sqrt{\frac{2(p - p_{\text{stat}})}{\rho}},$$

183 where p_{stat} is the static pressure (in hPa), ρ is air's mass density (in kg m^{-3}), v_{PPt} is the flow velocity
184 (in m s^{-1}), and p is the stagnation pressure (in hPa). According to the PPt's calibration certificate
185 an uncertainty of generally less than 1.5 % (at 1 m s^{-1}) is to be expected, which decreases to
186 $\sim$ 0.6 % at a flow velocity of 10 m s^{-1}.

3.4 The wind tunnel
187
188 The calibrations have been conducted in the horizontal wind tunnel of the JGU Mainz. This facility
189 (schematic in the electronic supplement, Fig. S 3) has a total length of 4.6 m and a circular outlet
190 opening of 0.64 m. The maximum achievable wind speed is approximately 20 m s^{-1} generated by
191 a 12-bladed impeller rotor in combination with a 14-bladed stator, both of which have an outer
192 diameter of 0.8 m. The rotor hub (0.4 m in diameter) is encased by a tapered cone downstream of
193 the stator to aerodynamically optimise the transition from the impeller housing (total length
194 1.25 m) to the flow channel (3.41 m length). The flow channel widens at 7° towards the horizontal
195 over a horizontal distance of $\sim$ 2.0 m. In the area of the maximum channel diameter, a gauze, and
196 a honeycomb mesh with a total thickness of 0.1 m are installed to laminarise the flow. Further
197 downstream, the flow channel diameter reduces via a radiused narrowing to compress the air
198 flow. The channel's outlet with a constant diameter of 0.64 m extends over a distance of 0.35 m.

3.5 Calibration setup and procedures
199
200 Generally, all setups for the TFS calibration were placed centrally within the wind tunnel's laminar
201 exit flow and in line with the tunnel's ring outlet edge to prevent potentially forming turbulence
202 from affecting the calibration.

3.5.1 TFS – PPt interactions

For exploring whether an extension of the UCASS by the TFS housing (with installed TFS) causes a measurable impact on the flow at the position of the UCASS optical detection region, a 3D-printed replica of the UCASS housing was used. Holes were drilled into the housing replica at two different positions along its longitudinal axis in order to 1) place the PPt inlet at the position of the optical detection area within the flow tube and 2) place the PPt inlet inside the TFS housing at the TFS's position while replacing the TFS. The replica housing was lacking all optical elements (laser diode, mirrors or photodiodes) that an operational UCASS comprises; all bulges along the flow tube's inner wall were evened out for this experiment.

Furthermore, a thermal anemometer (TA, by TSI Inc., model TSI 8455-300-1) was used to control the ambient flow generated by the wind tunnel. The TA was calibrated against the PPt in the free tunnel flow at flow velocities of 2 – 8 m s^{-1}. Then the experimental setup of the UCASS replica with integrated PPt was aligned iso-axially in the central flow of the wind tunnel. The experiments carried out are listed in Table 1.

The experiments were conducted at ambient wind tunnel air flows of $2 \leq v < 10$ m s^{-1} in increments of ~ 1 m s^{-1}. 10 individual measurements were averaged for each of the seven different wind speeds. The result of this experiments is shown in Fig. S 4 as correlations between TA-measured flow speeds (v_{TA}) against those from the PPt (v_{PPt}) within the UCASS flow tube. Notably, the UCASS tube flow velocity was generally increased compared to ambient wind speeds if the UCASS is iso-axially aligned with the ambient flow field, which was previously described by Smith et al. (2019) and confirmed during calibrations presented herein (see Sect. 4.2).

This experiment series demonstrate that applied modifications (extension of the flow tube geometry and implementation of the TFS) have hardly any measurable influence on the flow through a UCASS. At balloon ascent velocities, usually well below 10 m s^{-1}, none of the data series stood out from the statistical uncertainty. Therefore, the technical modification proposed herein is expected to have negligible impact on the measurement performance of the UCASS.

3.5.2 Cross sectional flow profile

For the following, a TFS housing shell without installed TFS was mounted on a UCASS to exclude any obstacle for the air stream through the flow tube. The PPt was attached near the outlet of the TFS housing so that the PPt inlet was iso-axially aligned and positioned as far as possible inside the flow tube along the longitudinal axis of the UCASS. Thus, along the setup's longitudinal axis, the PPt inlet was located at the point where the TFS would normally reside. The PPt was moved perpendicularly to the flow and in small increments ($\sim$1-2 mm) along a line between the two extremes of the flow tube's elliptical cross-section. The flow speed in the wind tunnel was kept constant, and for a single data point the average of 15 velocity measurements was taken at each PPt position. The profile measurements of the tube flow profile were carried out for a tunnel wind speed of about 5 m s^{-1} and 7 m s^{-1}.

Figure 3 shows corresponding results. The maximum standard deviation in PPt's position is estimated to be 0.2 mm and is shown together with the maximum standard deviation of the PPt data obtained from this series of measurements ($\sigma_{max} = 0.05$ m s^{-1}) in the bold-framed box. The position where the TFS would be aligned (if - except for this experiment – installed and adjusted by means of a positioning device) is marked by the grey-shaded area in Fig. 3. The flow profiles exhibit asymmetry. The boundary layer at the positive end of the y-axis seems broader than at its negative end. The reason for this is most likely the quasi-elliptic but asymmetric flow tube cross

247 section of the UCASS flow tube. As the ambient flow increases, an increased boundary layer
248 thickness is visible in the UCASS internal flow profile. Moreover, the flattening of the flow profile
249 is clearly visible towards the centre of the flow tube. For typical UCASS flow rates (here ~ 2-
250 10 m s^{-1}) this demonstrates, that at intended installation position (grey shaded area), the TFS flow
251 measurement occurs in the free tube flow of the UCASS. Notably, the determined cross-sectional
252 profile applies to a straight-line flow (i.e. the AOA equals zero). Under variable AOA (see Sect.
253 3.5.4) and at the selected TFS position any wall effects still have the least influence on the TFS
254 measurement compared to other positions along the tube's cross-section.

3.5.3 Iso-axial flow calibrations

256 With the iso-axially aligned setup (see beginning of Sect. 3.5) and with the PPt inserted from the
257 rear into the UCASS/TFS housing, such that the PPt inlet is positioned close to the TFS (cf. 3.5.2
258 and Fig. 2b), the flow calibrations were performed. The TA installed in the free wind tunnel flow
259 (outside the UCASS housing, see 3.5.1) was used to control the ambient flow speed.

260 The TFS calibration comprised a series of measurements at different flow velocities. From slightly
261 more than 0 m s^{-1} stepwise increasing flow velocities were set in the wind tunnel until ~ 10 m s^{-1}
262 was reached. About 25 measured values were recorded for the calibration of a single TFS. As
263 disturbance-related fluctuations occurred in the measured values during the calibration of both
264 the PPt and the TFS, 15 measured values were recorded for each of the sensors at each ambient
265 flow speed set. Mean values and standard deviations were determined from these PPt and TFS
266 data. Each TFS was calibrated individually, and the results of these calibration series are
267 summarised in Sect. 4.1 ff. After changing the TFS, the iso-axial and centred alignment of the
268 experiment setup at the wind tunnel outlet was frequently checked and readjusted if necessary.

3.5.4 Flow calibrations under variable AOA

270 For balloon soundings, the payload (incl. UCASS) is usually attached approx. 60 metres (via
271 unwinder, model "UW1" by Graw GmbH & Co. KG) below the balloon on a cord. The long cord is
272 intended to dampen the pendulum motion of the payload. Due to the vertical offset between the
273 balloon and the payload, also a horizontal offset between both ballon and payload occurs
274 depending on the horizontal wind speed. The balloon may lead the payload by a certain horizontal
275 distance, unless the horizontal wind speed is zero. Hence, during the balloon's ascent and with
276 horizontal winds the UCASS is likely inclined at a certain angle relative to the direction of vertical
277 lift. In addition, pendulum motion and rotations of the payload during flight cannot be completely
278 prevented, which can lead to a variable alignment of the UCASS relative to a straight ascent due to
279 several superimposed effects. Therefore, the impact of inclinations of the UCASS with respect to
280 the direction of flow on 1) the TFS calibration and 2) on the flow velocity within the UCASS is to
281 be quantified.

282 The experimental setup was aligned and positioned as described previously (beginning of Sect.
283 3.5). The iso-axial alignment corresponds to the zero position ($\varphi = 0°$, $\vartheta = 0°$). As the UCASS flow
284 tube is mirror-symmetrical along the vertical axis, the UCASS was horizontally inclined only along
285 the positive x-axis (φ) for changing AOA. Due to the quasi-elliptical shape of the UCASS flow tube,
286 the effects of the flow angle in y-direction (ϑ) were analysed for both the positive (UCASS inlet
287 points upwards) and the negative (UCASS inlet points downwards) deviation from zero. Figure 4
288 illustrates the measurement setup and provides an example of the angular distribution under
289 which the UCASS was aligned relative to the ambient flow field. Note, that the frame for holding
290 the UCASS/TFS setup also fixes the PPt (marked in Fig. 4a), which remains aligned with the UCASS
291 longitudinal axis and is positioned as close as possible at the TFS. Any angular change in the flow

292 direction to the UCASS inlet therefore affects the entire assembly (cf. Fig. 4c). At the beginning of
293 each measurement series, data were recorded for five different ambient flow speeds in the zero
294 position (0°, 0°) to verify the calibration curve of respective TFS used. The angles were then set
295 within the angle grid shown in Fig. 4b. 15 measured values of the PPt and the TFS were recorded
296 for five different tunnel flow speeds between about 3 and 7 m s^{-1} and the mean value with
297 standard deviation were determined from PPt and TFS data. The results are summarised in Sect.
298 4.3. An attempt was made to reproduce the set tunnel flow velocities for each measurement series
299 at varied AOA, which allowed also for investigating the relationship between the flow velocities
300 outside and inside the UCASS housing at variable AOA (see Sect. 4.4).

3.6 UCASS internal flow estimates

302 Besides the counted and classified particles, UCASS also records the particles' average beam
303 transit times (named MToF, Mean Time of Flight) in four different size ranges. In principle, these
304 beam transit times could be used to estimate the flow speed in the measurement volume and
305 therefore would provide another option for a sampling volume assessment. Such an approach is
306 used for example in connection with the particle detectors by Alphasense OPC-N2 and OPC-N3
307 (Bezantakos et al., 2020). We therefore correlated the measured TFS velocities with the inverse
308 of the different MToF values reported for each interval, when particles were detected. A
309 considerable number of apparently clipped values (piling at the apparent bottom and top end of
310 the measurement scale) were removed. Still, while there was a very weak correlation found
311 between the inverse MToF and the TFS, the huge variations, the clipped values and the scarcity of
312 data - in most 0.5 second intervals no particles are detected - prevent this approach from being
313 used as a measurement for a flow rate in UCASS.

4 Calibration results

315 To this point, it has been demonstrated that

316   1) the insertion of the TFS into the flow tube of the UCASS has no measurable impact on its
317   particle-sensitive area (Sect. 3.5.1) and
318   2) as the TFS installation is achieved by using a positioning device it is systematic for all TFSs
319   used whose measurements occur outside the tube's boundary layer in the central UCASS
320   flow.

321 Hence, the assumption seems appropriate that integrating TFS into the UCASS flow tube did not
322 generate any additional interferences for the calibrations discussed hereinafter.

4.1 High resolution (HRC) and three-point calibration (TPC) of the TFS

324 According to the functional relationship described in Eq. 1 the measured TFS output voltage is
325 calibrated versus the PPt-measured flow velocity, which is used hereafter as the calibration curve
326 of a TFS (further details in Sect. S 2 in the electronic supplement). For each measuring point, the
327 mean value plus (minus) the associated standard deviation - i.e. the extremes of variability - was
328 inserted into the calibration curve function yielding a deviation from the averaged measurement
329 point by not more than 0.08 m s^{-1} corresponding to a percentage maximum of 1.3 %. The results
330 show that the different TFS exhibit very similar behaviour and that the parameterisation of the
331 calibration curve function is valid for all calibrated TFS. Table S 1 (see electronic supplement) lists
332 the parameterisation coefficients for the TFS analysed in the calibration results. Repeated
333 calibration series with a larger time offset and with the same TFS after disassembly/reassembly
334 of the setup also reproduced previous values within 1.8 % at maximum, and on average within

335 1 %, in the relevant range of ambient flows. However, the measurements of the calibration curves
336 were likely influenced by the ambient temperature and pressure conditions in the laboratory as
337 both affect air's mass density, which in turn controls the heat advection at the TFS.

338 In the process of these high-resolution calibrations (calibrations with up to 25 data points and in
339 the following denoted as HRC) and analyses of the calibration curves, it was found that only three
340 calibration points (at ~2, 5, 8 m s^{-1}) reproduce the calibration curve with acceptable accuracy (see
341 electronic supplement, Sect. S 2, for details). For the TFS used (here: TFS 8), and at tunnel flow
342 speeds between 2 and 8 m s^{-1}, the three-point calibration (in the following denoted as TPC) curves
343 did not deviate by more than 1 % from the highly resolved initial calibration curve.

4.2 Internal versus external flow velocity

345 The PPt was repositioned next to and slightly upstream of the UCASS inlet to measure in the free
346 flow of the wind tunnel (setup is shown in Fig. S 5). The UCASS-integrated TFS 8 had previously
347 been calibrated with the PPt to have a calibration curve (TFS 8.2 (TPC) see Table S1) under the
348 same laboratory conditions as the experiment. The UCASS was aligned iso-axially to the ambient
349 flow of the wind tunnel and centred at the annular outlet of the tunnel. The wind tunnel flows
350 were stepwise increased from slightly more than 0 to up to 11 m s^{-1} and then decreased with a
351 total of 17 different settings. For each of the ambient flow speeds, 15 velocity values were
352 recorded as measured by the PPt to be averaged. In Fig. S 6, the PPt-measured flow velocity
353 outside the UCASS is displayed in reference to the UCASS internal flow velocity determined with
354 the TFS 8. The velocity range relevant for balloon soundings (2 - 8 m s^{-1}) is indicated by the black
355 dashed square.

356 Within this range, 10 different values of ambient flow speed were set for each measurement of
357 this series. The standard deviation σ of the PPt data range between 0.01 and 0.04 m s^{-1}. Only the
358 mean value of the TFS output voltage was noted, which resulted from the automated averaging by
359 the multimeter used. During the TFS 8 calibrations, standard deviations of at the most 0.08 m s^{-1}
360 were obtained corresponding to a maximum relative deviation of 1.3 % (extremes of variability,
361 cf. first paragraph in Sect. 4.1). A first-order polynomial fit was created for the recorded
362 measurement. The resulting line-fit indicates that in an iso-axial arrangement the UCASS internal
363 flow velocity exceeds the outside flow speed. Calculated from 10 data points at external wind
364 velocities between 2 and 8 m s^{-1}, the UCASS internal flow velocity is increased by 10.7 to 11.9 %,
365 with an average relative deviation of 11.3 %, as compared to the external flow speed.

366 This result quantitatively compares well with the results of Smith et al. (2019), who simulated an
367 increase in the UCASS internal flow velocity by 12 % under an iso-axial alignment of the UCASS
368 and at an ambient flow speed of 5 m s^{-1}. Taking into account the standard deviations of averaged
369 data points determined here may put the small deviation between previous and current results
370 into perspective.

371 However, in balloon-borne UCASS field applications, the balloon ascent rate is usually used to
372 determine the sample volume flow and thus the measured particle number concentrations (e.g.
373 Kezoudi et al. (2021)). So, when a UCASS was iso-axially aligned during a straight balloon ascent
374 at rates of 2 to 8 m s^{-1}, the GPS or pressure-based calculation would lead to an underestimated
375 UCASS sample volume flow by about 11-12 % and the particle number concentrations would be
376 overestimated accordingly. Therefore, from current point, a direct measurement of the UCASS
377 internal flow velocity during flight appears useful, but as will be shown (Sect. 5), the conditions

378 during balloon soundings are more complex and the necessity for a flow velocity detector
379 integrated into the UCASS gets all the more obvious.

4.3 UCASS internal flow velocity under variable AOA
381 Compared to previous experiment series, the UCASS was intentionally misaligned from the iso-
382 axial orientation (cf. Sect. 3.5.4).

383 Figure 5 shows the highly resolved calibration curve TFS 8. The mean values from experiment
384 series at five ambient flow speeds are also depicted for each AOA. The standard deviations are not
385 shown for the sake of clarity of the figure. The error in setting the UCASS deflection angle was
386 estimated to be ±0.5° in each case. In the zero position (0°, 0°), which was calibrated once at the
387 beginning and at the end of the series, the σ-values ranged between 0.002 and 0.003 V (TFS 8
388 output voltage) or between 0.02 and 0.04 m s^{-1} (PPt). With increasing AOA, the standard
389 deviations (σ) rose to a maximum of 0.025 V (TFS 8) and 0.09 m s^{-1} (PPt). Hence, the fluctuations
390 of measured variables generally increased with increasing AOA.

391 Based on the TFS 8 calibration curve, the flow velocities $v_{\text{TFS}}^{a}(U)$ were determined with the mean
392 TFS output voltage values ($\overline{U}$). These are compared with the flow velocities $v_{\text{TFS}}^{b}(U)$ resulting from
393 the extreme values of standard deviation at each mean output voltage (i.e. $\overline{U} \pm \sigma$). The maximum
394 standard deviation range observed was ± 0.31 m s^{-1} (8.3 %). Oscilloscope records of the variations
395 in the TFS output voltage over 20 s clearly indicated an increasing scatter intensity when varying
396 the AOA of UCASS, e.g. from (0°, 0°) to (20°, -40°). The output voltage fluctuations were invariant
397 in time (in particular non-periodic) and stationary, i.e. rather of a statistical nature.

398 The mean values of the TFS measurements were inserted into the calibration curve function of
399 TFS 8 to determine the flow velocities (v_{TFS}) to be juxtaposed to the mean PPt-measured flow
400 velocities (v_{PPt}). The flow velocity determined with the calibration curve was used as the reference
401 and an error is considered with

$$\varepsilon = \frac{v_{\text{TFS}} - v_{\text{PPt}}}{v_{\text{TFS}}} \cdot 100, \qquad\qquad 4$$

403 out of which the maximum percentage error and its mean resulted for each AOA. Table 3 shows
404 the maximum and the mean of the relative percentage deviation of measured values at variable
405 AOA compared to the calibration curve TFS 8. At AOA of up to 30°, the maximum relative
406 percentage deviation was 3.5 %, and above 30°, the relative percentage deviation of measured
407 values from the calibration curve increased significantly. At such large AOA, the σ of TFS-
408 measured voltages also rose substantially. During balloon sounding, UCASS inclinations of more
409 than 30° from the vertical are not expected. In an earlier study (Smith et al., 2019), a model was
410 used to simulate the angular inclination of the UCASS in relationship to the direction of ascent.
411 Initial pendulum oscillations of up to ± 20° were assumed, which were damped to around ± 5°
412 within about 30 seconds. If these conditions occurred at an actual balloon sounding with UCASS,
413 the percentage relative deviation of measured velocities as determined here (based on the TSF 8
414 calibration curve) would be a maximum of 2.8 % under variable AOA smaller than 20°. Hence,
415 even at UCASS inclinations of up to 20°, the particle concentration is affected by this angle
416 deflection with a maximum uncertainty of less than 3 % (maximum relative deviation). To validate
417 the TFS 8 data series, the measurements were repeated with TFS 7 in the same setup.
418 Corresponding results are summarised in Sect. S 3 (electronic supplement) representing a
419 qualitative and largely quantitative confirmation of the results and conclusions made.

4.4 Internal versus external flow velocity under variable AOA

In Fig. 6, the velocity of TA-measured ambient wind tunnel flows (as reference) is plotted against the PPt-measured flow velocity inside UCASS. Standard deviations of 0.01 to 0.10 m s^{-1} were determined for the ambient flow velocity between 2 and 8 m s^{-1}. For PPt data, σ-values ranged from 0.02 to 0.09 m s^{-1}, which increased with rising ambient flow velocities and AOA. With increasing AOA, the UCASS-internal flow velocity decreased. For AOA of (0°, 30°) and (0°, -30°), and beyond, the UCASS-internal flow was slower compared to external flow velocities.

The UCASS-internal flows in zero-position (0°, 0°) were used as reference and parameterised by a first-order polynomial fit. The comparison of a) the calculated flow velocity inside the iso-axially aligned UCASS with b) its internal flow velocities at AOA of (0°, 30°) and (0°, -30°) revealed a relative percentage decrease in the flow velocity of around 15 % (see Table 4). For an iso-axially aligned UCASS, the internal flow is accelerated by on average ∼ 11.3 % (see Sect. 4.2). The contrary effects of a) a flow acceleration inside the iso-axially aligned UCASS and b) the deceleration inside the UCASS when deflected from the zero-position are likely superimposed. Thus, with a UCASS inclination of 30° during a balloon sounding, the internal UCASS flow velocity is reduced by around 4 % net compared to the external flow. In turn, at such UCASS inclination, a particle number concentration calculated with the GPS or pressure-based ascent velocities underestimates the prevailing trace material concentrations by only about 4 % under these conditions.

At a certain deflection angle (30°, 0°) a noticeable but undeterminable interference effect appears to have impacted the laboratory experiments. With increased deflection of the UCASS, the inlet opening of the UCASS is shifted out of the central wind tunnel flow and towards the tunnel's wall. With decreasing distance to the wall of the wind tunnel, effects of flow disturbances cannot be ruled out, which could influence the relative deviation from the calibration curve. Potentially, signal fluctuations are also amplified by flow disturbances that occur at the leading edge of the UCASS entrance when the UCASS is deflected too far from the zero-position. The TFS appears to be sensitive to such fluctuations. In addition, an influence of wind gusts on the experiment cannot be excluded, as the wind tunnel is operated inside a building, but has connections to the building's exterior to enable enhanced wind tunnel flows.

5 Ambient measurements

Ambient balloon soundings were carried out with two UCASS instruments, such that two TFS were operated in parallel during respective ascent. The balloons' ascent rate is determined from both the static pressure measurement (v_p) and the GPS data, each of which is recorded independently. The static pressure in flight, resolved at 1 Hz, is converted to barometric altitudes by the internal primary data processing in the VAISALA sounding system, as recalculations (based on Sonntag (1994)) confirm. GPS and pressure-derived ascent rates correlate very well (regression yields a slope of one and a constant element of - 0.1 m s^{-1} with a coefficient of determination r^2 of 0.99).

5.1 Vertical profiles

Figure 7 shows vertical profiles of three balloon soundings launched from Tailfingen (Germany), at ∼ 900 m above sea level (a.s.l.) in August 2023. The profiles allow for comparing 1) the balloon ascent rate from the GPS measurements v_{GPS}, 2) the balloon ascent velocity from the static pressure measurements v_p, and 3) the flow velocities through the two UCASS units (TFS A and TFS B) operated on each ascent. Results from other balloon soundings are shown in the electronic

463   supplement (Fig. S 10). The TFS used for the balloon soundings and their calibration coefficients
464   are listed in Table S3. The profiles are limited to an altitude of 7.5 km a.s.l., as at about this height
465   the ambient temperatures fell below the specified temperature limit (253 K, see B+B-Thermo-
466   Technik (2016)). Further laboratory tests are required to confirm the robustness of the TFS
467   measurements also at temperatures of 253 - 220 K or to reveal the need of further corrections. As
468   nearly all UCASS particle measurements were detected below 7.5 km, the restricted height range
469   nevertheless covers the relevant part of the flight. The data are low-pass filtered by a 10-second
470   running average.

471   A common feature of the vertical profiles is the stronger scatter of the GPS-derived ascent rates
472   compared to those based on pressure measurements. This might be connected to a larger
473   uncertainty inherent with the GPS. In general, however, both values are well-correlated. Up to
474   ~ 2 km of the balloon sounding of 12 August (Fig. 7a) the TFS measurements agree relatively well
475   with GPS and the pressure data (see also Fig. 7b). Below~ 3 km, TFS A and TFS B deviate from the
476   pressure and GPS data by up to 30 %. Up to ~ 3.8 km, the different speed measurements from all
477   instruments are comparatively consistent. Above 3.8 km, the TFS measurements (again consistent
478   between TFS A and B) show periodically fluctuating and lower flow speeds (by up to 15 %, and
479   above 7 km altitude by up to 25 %) compared to those resulting from GPS and pressure.

480   During the earlier balloon sounding of 16 August (Fig. 7d) and up to an altitude of ~ 2.4 km, the
481   TFS-based velocities are systematically higher (in peaks by up to 45 %, cf. Fig. 7e) than
482   corresponding values from GPS and pressure. In contrast to the previous case, the measurements
483   of the four sensors are quite consistent at altitudes between 2.4 and 5.3 km with deviations of
484   seldomly more than ± 10 %. Above ~ 5.3 km, the two independent TFS measurements, which
485   correlate quite well with each other, both deviate increasingly from the GPS and barometric data
486   with increasing altitude and show up to 15 % lower UCASS flows compared to the balloon ascent
487   rates.

488   The balloon sounding on the afternoon of 16 August (Fig. 7g) shows a more or less satisfactory
489   match between all four independent measurements only at the lowest altitudes (up to ~ 1.3 km).
490   Between 1.3 and 2.7 km, the TFS- velocities are generally higher (on average by 15 %, in peaks up
491   to 25 %, cf. Fig. 7h) than those derived from GPS and pressure. Above 3.2 km, reversely the ascent
492   velocities from pressure and GPS slightly exceed the TFS data. At altitudes of 4.5-5.5 km and above
493   ~ 6.2 km, GPS and pressure measurements commonly reveal increased vertical velocities that rise
494   from about 6 m s^{-1} to about 8 m s^{-1}. Within these layers TFS-velocities are mostly 15 % (in peaks
495   up to 25 %) slower than the ambient air flow. The origin of these features in the GPS and pressure-
496   based velocity profile apparently has, if any, only minor impact on the TFS measurements.

497   These examples suggest that over large parts of the vertical sounding (up to 7.5 km altitude) the
498   flow velocity within the UCASS (and thus through its optically sensitive particle detection region)
499   does not match the GPS or p-derived ambient flow velocity. For each of the vertical soundings
500   shown in Fig. 7, the speeds of the horizontal wind components (u and v) and the sum of both as
501   total wind speed are also displayed in vertical profiles (Fig. 7 c, f, i). Occasionally, changing wind
502   speeds appear to be reflected in changing velocity ratios (e.g., the decrease in u at 4 km and 6 km
503   in Fig. 7c or the features in u at 5 km in Fig. 7f and at ~ 6 km in Fig. 7i), which would indicate a
504   certain correlation. However, a general causality between changing wind speeds and the ratio of
505   TFS-based to p-based flow velocities through the UCASS cannot be inferred without knowledge of
506   the actually resulting AOA at which the UCASS are sampling. Besides wind speeds, also stability
507   (Brunt-Väisälä frequency N^2), turbulence (Richardson number, Ri), and wind shear as function of

508 altitude (not shown herein) were investigated concerning their potential relationship with the
509 variable velocity ratios, but none of general validity could be identified.

5.2 Implications of observed features

511 Influences on the UCASS-internal flow speed and pattern due to an additional installation of a TFS
512 in a housing extension, if any, are negligible (Sect. 3.5.1). The sensitive area of the implemented
513 TFS is located within the free tube flow through a UCASS, i.e. outside the boundary layer of the
514 UCASS flow tube's inner walls (Sect. 3.5.2). Moreover, with an iso-axial alignment of the UCASS,
515 the inner flow is accelerated by ~ 11.3 % when compared to the ambient flow velocity around the
516 UCASS (Sect. 4.2), which is in general agreement with earlier findings (Smith et al., 2019). As
517 discussed in Sect. 4.4, with increasing angular deflection of the UCASS from the iso-axial
518 orientation, the flow velocity inside a UCASS is decelerated towards values of the ambient flow
519 speed and below.

520 The payload as used during the field mission had a total weight of up to 3.9 kg. About 10,000 litres
521 of helium are required for the balloon to yield enough buoyancy for desired lift. Under conditions
522 with horizontal winds, the effective surface area of the filled balloon is many times larger than
523 that of the payload structure (<0.1 m^3). When fully unwound, the flexible cord between the
524 balloon hull and the payload extends up to ~ 60 m. During its ascent from the ground through the
525 boundary layer, the balloon hull (with a larger surface area compared to other components of the
526 balloon assembly, which is moreover located several dozen meters above the payload) is
527 frequently exposed to varying wind speeds (cf. Fig. 7). With increasing altitude and decreasing
528 ground friction, the (variable) wind shear increases equally. Therefore, during its ascent, the
529 balloon assembly generally tilts relative to the vertical as soon as horizontal wind speeds other
530 than zero prevail, as shown by the horizontal displacement between two radiosondes at opposite
531 ends of a balloon payload ensemble with a total length of ~62 m (see Sect. S 4 in the electronic
532 supplement).

533 Above the boundary layer, the balloon's much larger surface area may cause it to act as a sail in
534 prevailing horizontal winds, causing the payload with a much smaller surface area to be towed
535 behind. Therefore, the balloon is most times slightly dislocated with respect to the resultant wind
536 vector compared to the payload, the payload will inevitably be inclined relative to the wind vector
537 over large parts of the balloon sounding.

538 Based on the ratios of the TFS measurements compared to the ascent velocities from GPS and
539 pressure measurements, different scenarios arise over a flight, in which

540   1. The flow velocities through the UCASS are increased compared to the ascent velocities: as
541   if the deflection angle of the UCASS relative to the vertical was comparatively small or
542   close to an iso-axial alignment of the UCASS within the ambient flow,
543   2. The flow velocities through the UCASS are within the variability range of the GPS and
544   pressure measurements of the ascent velocities: for this, a deflection of the UCASS of
545   about 20°-30° would have to be attained (cf. Fig. 6 and Table 2) while an enhanced
546   uncertainty is hereby accounted for by using the TA instead of the PPt for measuring the
547   wind tunnel flow speed, as the PPt measured at that time inside the UCASS housing,
548   3. A flow velocity through the UCASS that is smaller than the GPS or pressure-based ascent
549   velocities: for this, a deflection of the UCASS of about >30° would have to be reached.

For the last of these points in particular, the required deflection angles of the UCASS appear extreme to clearly explain observed velocity ratios. In addition, pendulum movements of the payload around a position in the inclined state (i.e. without swinging through the pendulum's equilibrium, which would correspond to an iso-axial, strictly vertical UCASS alignment) could generate a continuously variable orientation of the UCASS in the flow. Moreover, it was observed that the payload can rotate around its vertical axis (in line with the balloon cord). The superposition of these movements and others resulting from the variability of the payload's lift (e.g. indicated by fluctuations in GPS and pressure-based ascent rates) may lead to various influences on the flow through the UCASS, which currently are neither separable nor quantifiable. As the ascent speed is mainly determined by the balloon's buoyancy, drag force, and gravitation, the resulting wind situation at the payload may differ from that at the balloon due to small scale atmospheric variability (e.g. turbulence).

During balloon soundings, the flow velocity through the UCASS is subject to complex influences and is largely decoupled from the pure vertical velocity (i.e. the ascent rate) of the balloon. The high variability of the flow velocity measured during ascent directly inside the UCASS emphasises the importance of such a direct measurement. The frequent deviation of the UCASS flow speed from the GPS or pressure-based vertical velocity is one further argument in favour of implementing an independent flow sensor inside the UCASS. The GPS or pressure-based ascent rates deviate by values in the range of metres per second from the UCASS internal flow velocity. Based on a velocity of 6 m s^{-1}, a deviation by ± 0.5-2 m s^{-1} results in an error of ± 10-30 % and a corresponding over- or underestimation of the resulting particle number concentration.

Table 5 summarises the main uncertainties arising from the different methods for determining a flow velocity through UCASS and which have equal quantitative impact on resulting particle number concentrations. From the Gaussian error propagation of the relationship given in Eq. 1 and Eq. 2 an overall uncertainty $\Delta v_{\text{TFS}}^{\text{corr}}$ combines from 1) the uncertainties in T and p measured with a radiosonde RS 41 SGP (Vaisala, 2024) also including uncertainties arising from the TFS calibrations conditions (in p_0 and T_0) and 2) the uncertainty Δv_{TFS} (i.e. determined σ) obtained from the cold chamber test at different ambient temperature conditions (cf. Sect. S 1 in the electronic supplement). For three chosen temperatures (i.e. 275 K, 264 K, and 254 K) from these chamber experiments the corresponding deviations of the GPS-based flow velocities (Δv_{GPS}) from corresponding $v_{\text{TFS}}^{\text{corr}}$ are determined at equal temperature conditions during three vertical soundings (Fig. 7 and adjacent text). Thus, the total uncertainty in $v_{\text{TFS}}^{\text{corr}}$ is fairly consistent within a range between 6.9 % and 8.8 % (values marked in grey in Table 5). In a few of the conditions selected here (275 K and 264 K), resulting Δv_{GPS} is comparatively low (values framed between two vertical lines in Table 5), or in almost similar range of $\Delta v_{\text{TFS}}^{\text{corr}}$ (values framed between two horizontal lines) however, in other cases (enclosed framed values) the offset in v_{GPS} is significant and can exceed 30 % (occasionally even more as seen in Fig. 7d). In essence, v_{GPS} appears as the more precise measurement, but can unpredictably become highly inaccurate upon vertical sounding over large height ranges (500 - 1500 m). In contrast, $v_{\text{TFS}}^{\text{corr}}$ presumably is the more accurate measurement over discussed vertical range up to ∼ 7.5 km, with a comparatively higher though determinable imprecision.

6 Summary and Conclusions

This study indicates a possible improvement of the Universal Cloud and Aerosol Sounding System (UCASS), a balloon-borne optical particle counter, to obtain aerosol and cloud droplet concentration measurements with increased accuracy. The integration of a thermal flow sensor (TFS) into the UCASS allows for direct, real-time and continuous flow velocity measurements in the immediate vicinity of UCASS's particle detection region. This approach resolves inaccuracies arising from the conventional reliance on GPS or pressure-based balloon ascent velocities, which do not account for gusts or strong wind shear, payload oscillations, flow distortions (caused by the UCASS housing), and particularly the deflection of the UCASS body from an iso-axial alignment during ascent.

Wind tunnel experiments showed that the UCASS-internal flow velocity, when iso-axially aligned with the ambient airflow, is on average 11.3 % faster than the surrounding external flow (between $2 - 8$ m s^{-1}), largely consistent with previous investigations. Hence, the airflow dynamics of the UCASS are reproducible and predictable under controlled conditions. Further laboratory experiments under variable angles-of-attack (AOA) revealed that with a deflection of the UCASS by around 20° - 30°, the UCASS-internal flow velocity is reduced to values approximately corresponding to the external flow velocity.

It was found that high-resolution calibrations of a TFS provide accurate results that are parameterizable according to King's Law, with deviations of no more than 1.3 % from the mean samples. A more efficiently implementable three-point calibration (TPC) method (using flow velocities of approximately 2 m s^{-1}, 5 m s^{-1}, and 8 m s^{-1}) showed deviations of less than 2.9 % compared to detailed calibrations.

During balloon soundings, UCASS-internal flow velocities could deviate significantly from the GPS or pressure-based ascent rates, varying by up to 30 %. Thus, accurate measurements of particle concentrations based solely on GPS or p-derived ascent rates are subject to considerable uncertainty. Vertical profiles from three soundings up to 7.5 km (see Sect. 5) showed that the deviations in flow velocity increased with increasing altitude due to changing atmospheric conditions and balloon-payload-geometry (i.e., the inclination of the payload orientation and thus the UCASS alignment). Referring to the thought model of the balloon sounding (see Sect. 2), that the flight pattern of the balloon is driven by the horizontal wind components (i.e. u and $v > 0$): then 1) the balloon body acts as a sail with its comparatively large surface and 2) the comparatively small payload is towed. In other words, even if the main wind components with respect to the payload's inertial system (u_{rel}, v_{rel}) were nearly zero, this will typically result in a constellation of the balloon-payload geometry which causes a flow towards UCASS with a non-zero AOA. While UCASS is aligned with the cord to the balloon, it is deflected with respect to the buoyancy-induced vertical lift, i.e., iso-axial flow to the UCASS is rarely given. The actual flow, which is affected by the pendulum motion and rotation of the payload and their superposition, is hardly reproducible or quantifiable. This ultimately underlines the need for a continuous measurement of the actual internal UCASS flow during the entire flight.

Hence, for airborne particle measurements the calculated particle concentrations from UCASS detections based on GPS or pressure ascent rates may introduce errors of up to 30 %. Real-time TFS data would reduce this uncertainty by ensuring that the actual air volume of the samples is determined independently of external conditions. The integration of the TFS into the UCASS therefore represents an improvement in the methodology of measuring aerosol and cloud droplet concentrations up to 7.5 km. By providing direct and precise flow velocity

measurements, the TFS avoids the limitations of GPS or p-based methods, including errors caused by payload movements, gusts, wind shear, and flow deviations caused by the shape of the UCASS housing. Field tests confirmed that this approach leads to more accurate assessments of air volumes in the samples and can reduce uncertainty in calculating particle number concentrations.

The knowledge gained may motivate future modifications and improvements in the further development of the balloon-borne UCASS instrument. The robust three-point calibration methods applied in this study facilitate the technical effort involved in integrating TFS into a modified UCASS. This work can provide a basis for improved vertical profiling of aerosols and cloud elements with cost-effective and flexible instruments such as UCASS.

Code and data availability
Both data and the program code are available in a repository via
"https://doi.org/10.5281/zenodo.15519552".

Author contribution
SJ performed the calibrations, reporting and optimised technical designs. SJ, RW, KK wrote the article with contributions by JG, CS, WS, LKE, LV and HT. LV, LKE and CvG ensured the technical operability of the TFS-equipped UCASS instruments (supported by JG, CS, WS) and the balloon gondola during field missions. HT (forecasting), LKE (preparation and launch) and KK, SJ (recovery) contributed invaluably to successful balloon soundings.

Competing interests
The authors declare that they have no conflict of interest.

Acknowledgements
The contributions from the technical staff at the workshops of the Institute for Physics of the Atmosphere (Mainz University) and of the MPI for Chemistry were crucial and essential. In particular, we acknowledge the support of H. Rott, K. Wilhelm, M. Maurer, T. Böttger, P. Schumann, T. Kenntner, M Dietrich, and B. Meckel. We furthermore gratefully acknowledge the excellent support by R. Dominik, I. Knapp-Wagner, J. Frielingsdorf, M. Euler, and O. Krause as well as the radiomen (a. o.) W. Hallmann (DF7PN), R. Roth (DG7FDE). We are also deeply grateful for the generous hospitality of M. & A. Conzelmann (Tailfingen) of A. Lampmann (BSC Spielberg), and the residents of Spielberg. The authors thank the Editor (EDITORNAME) and (NUMBER) (anonymous or NAME) reviewers for their careful evaluation of this article and their valuable and constructive recommendations.

Financial support
Our research was funded by the Deutsche Forschungsgemeinschaft (DFG, German Research Foundation) – TRR 301 – project ID 428312742, in the subproject B02 "BISTUM" within the CRC entitled "The Tropopause Region in a Changing Atmosphere" ("TPChange"). We also received financial support by the "Dres. Göbel Climate-foundation".

Figure captions
Figure 1: Design of the UCASS and arrangement of its optical elements. Figure (a) shows the side view of the UCASS, while figure (b) shows the front view. The definition of the particle detection zone (df1) has been added to the figure. Adopted from Smith et al. (2019).

Figure 2: (a) The TFS housing ("c1"), which also contains the control and regulation electronics of the TFS. The sensitive area of the TFS with a length of 6.9 mm is labelled as "c2". (b) The frontal

679 view of the experimental setup. The perspective is in the direction of flow towards the UCASS front
680 and into the flow tube, looking at the TFS and the Prandtl-Pitot tube, which is located downstream
681 behind the TFS.

682 **Figure** 3: Resulting flow velocity profiles along the elliptical cross-section of the instrument's flow
683 of the UCASS or of the TSF housing with a diameter of 40 mm × 30 mm (length × width). Along the
684 cross-section's main axis, the flow velocity measurements were carried out; twice for an ambient
685 flow velocity of $\sim$ 5 m s^{-1} (forwards "a" and backwards "b", respectively) and once for $\sim$ 7 m s^{-1}
686 (direction "b" only). Each data point represents an average of 15 velocity measurements. The
687 error bars, which are shown representatively in the bold-framed box, show the maximum
688 standard deviation for PPt's position (σ_{max} = 0.2 mm) and for all flow velocities measured with the
689 PPt (σ_{max} = 0.05 m s^{-1}). The position of the TFS (if installed) is marked by the grey area.

690 **Figure** 4: Measuring setup with UCASS, mounted TFS housing, and installed PPt (from the rear
691 reaching into the TFS housing), fixed in a vertically and horizontally tiltable apparatus with scales
692 for reading the deviation angles in each direction a) Side view in horizontal orientation b) Variable
693 deviation angles, which were set in angular degrees deviating from the zero position (iso-axial
694 case) during the experiments c) View of the measuring setup under horizontal and vertical
695 displacement from the zero position.

696 **Figure** 5: Comparison of the high-resolution calibration curve (HRC) with measurements of the
697 UCASS-implemented TFS 8 at variable angles of attack. The standard deviations of individual data
698 points are not shown for the sake of clarity.

699 **Figure** 6: Comparison of the recorded flow velocities outside (v_{TA}) and inside (v_{PPt}) the UCASS at
700 variable angles of attack during the series of measurements with TFS 8. The standard deviations
701 (at the most ± 0.1 m s^{-1} at tunnel wind speeds between 2 and 8 m s^{-1}) are not shown for reasons
702 of clarity. First-order polynomial fits were created for the flow velocities recorded under various
703 angles of attack to compare with the high-resolution calibration (HRC) at zero position (0°,0°).

704 **Figure** 7: Vertical profiles of the vertical velocity based on measurements of changed GPS and
705 barometric altitudes per unit time (i.e. v_{GPS} and v_p) and on TFS measurements of the flow velocity
706 (v_{TFS}^{corr}) through the UCASS of selected balloon soundings during a field mission together with
707 observed horizontal wind data (*u* and *v*) and the total wind speed (*u* + *v*) a-c) from 12 August,
708 launch at 14:10 (LT), d-f) from 16 August, launch at 11:51 (LT) and g-i) from 16 August, launch at
709 13:41 (LT). 10-seconds-running average of respective data are shown. Additionally, respective
710 deviations of the differently obtained flow velocities from each other are shown for each vertical
711 profile (panels b, e, h). Note that the deviation of the ascent rates (i.e. the external flow velocity,
712 GPS or *p*-based) in reference to the UCASS-internal flow speed differs from zero over large parts
713 of depicted flight sections. Occasional correlations of changing velocity ratios with changes in
714 wind speeds are recognizable, but a general causality cannot be identified.

715

716

717

718

719   Figures

720

721

722

723

724

725

726

727

728

729

730

731

732

733

734

735

736

737

738

739   Figure 1

740

741

742

743

744

745

746

747

748

749

750

751

752

753

754

755

Figure 2

765

766

767

768

Figure 3

788

789

790

791

792

793

794

795

796

797

798

799

800

801

802

803

804

805

806

807

Figure 4

809

810

811

812

813

814

815

816

817

818

819

820

821

822

823

824

825

826

827

828

Figure 5

829

830

831

832

833

834

835

836

837

838

839

840

853 Figure 6

854

855

856

857

858
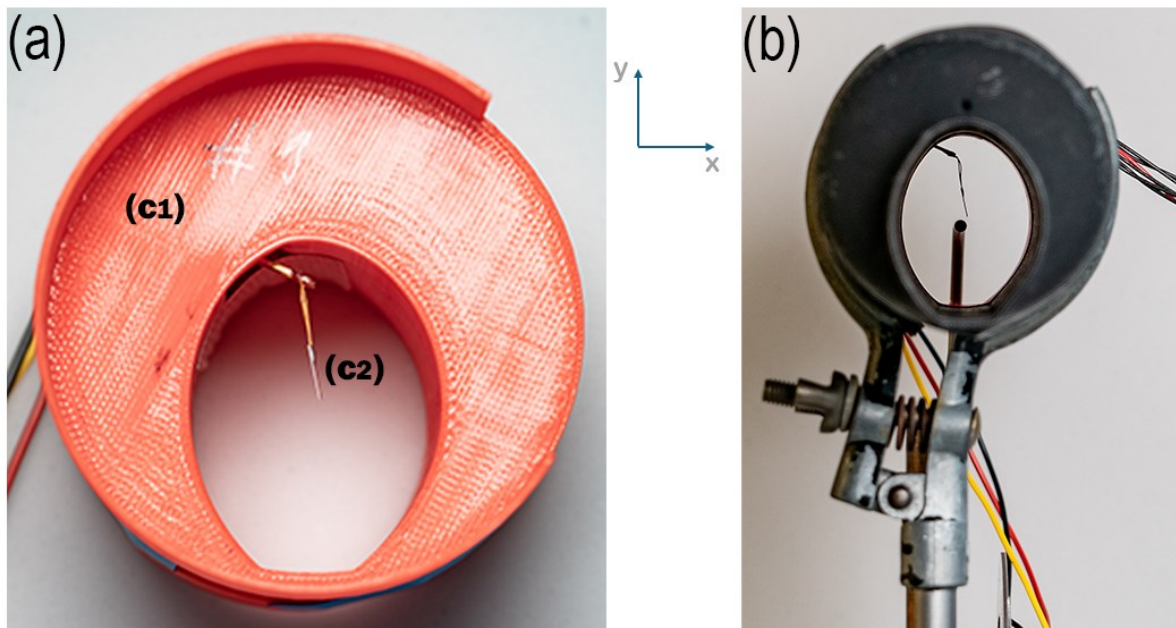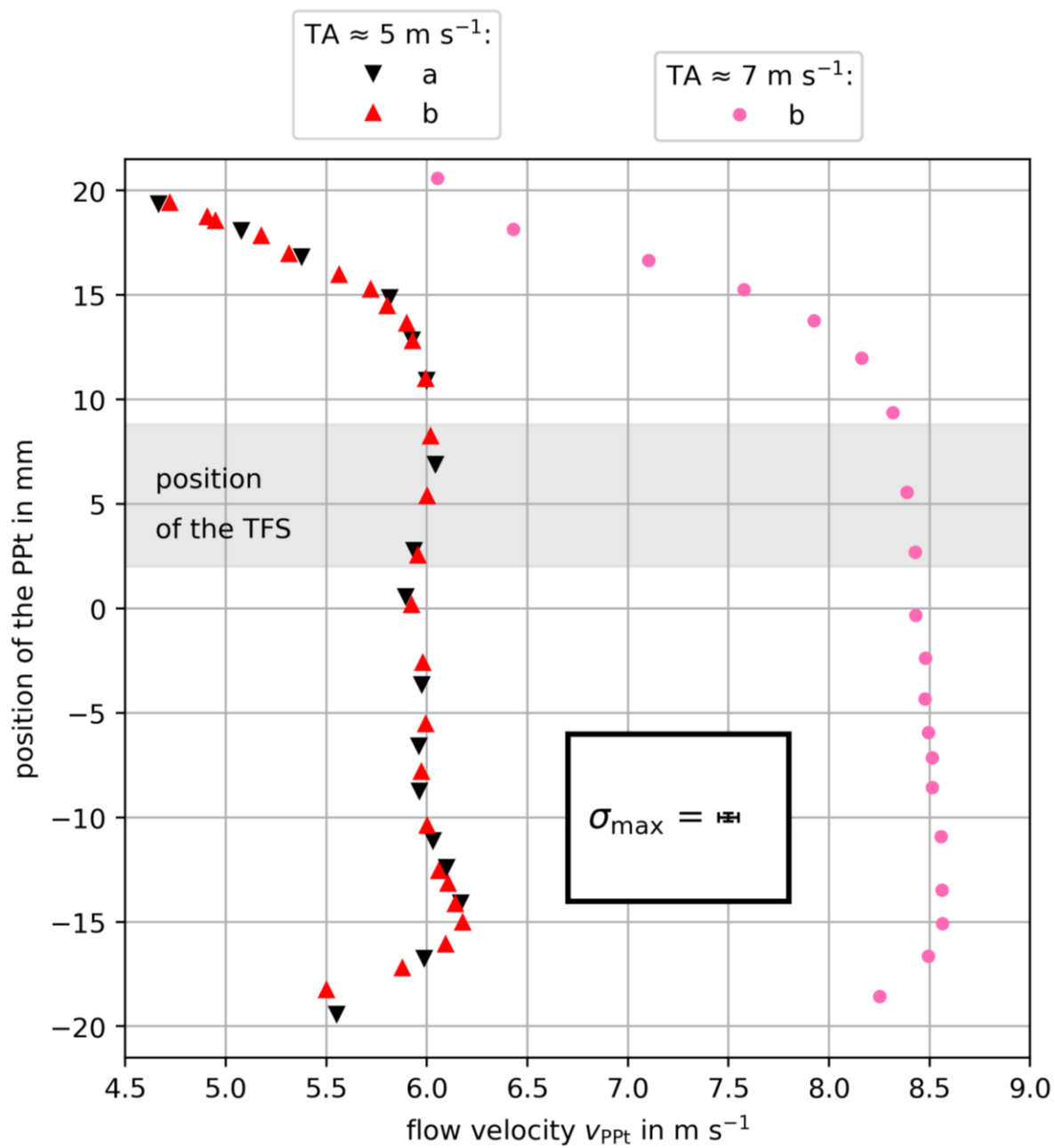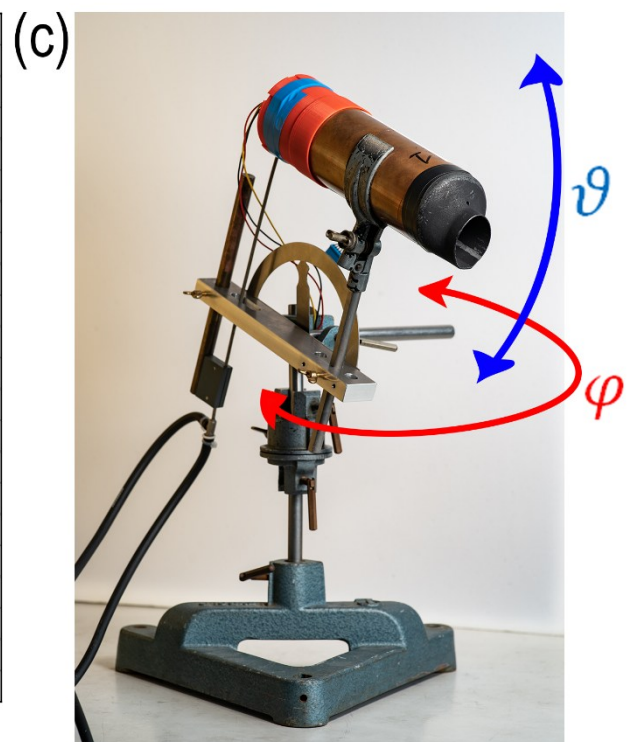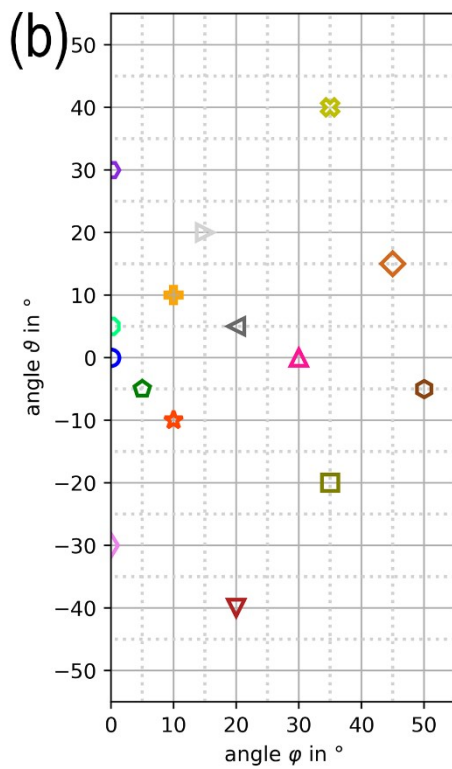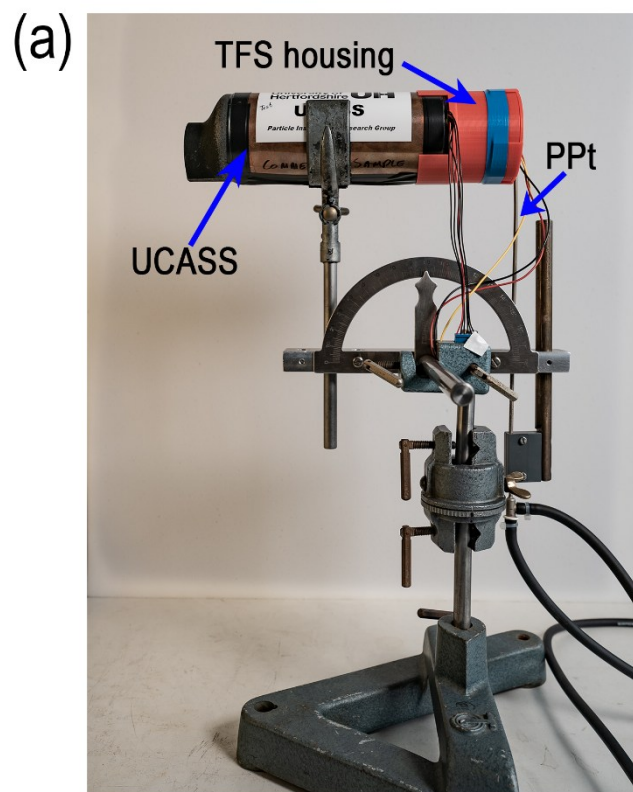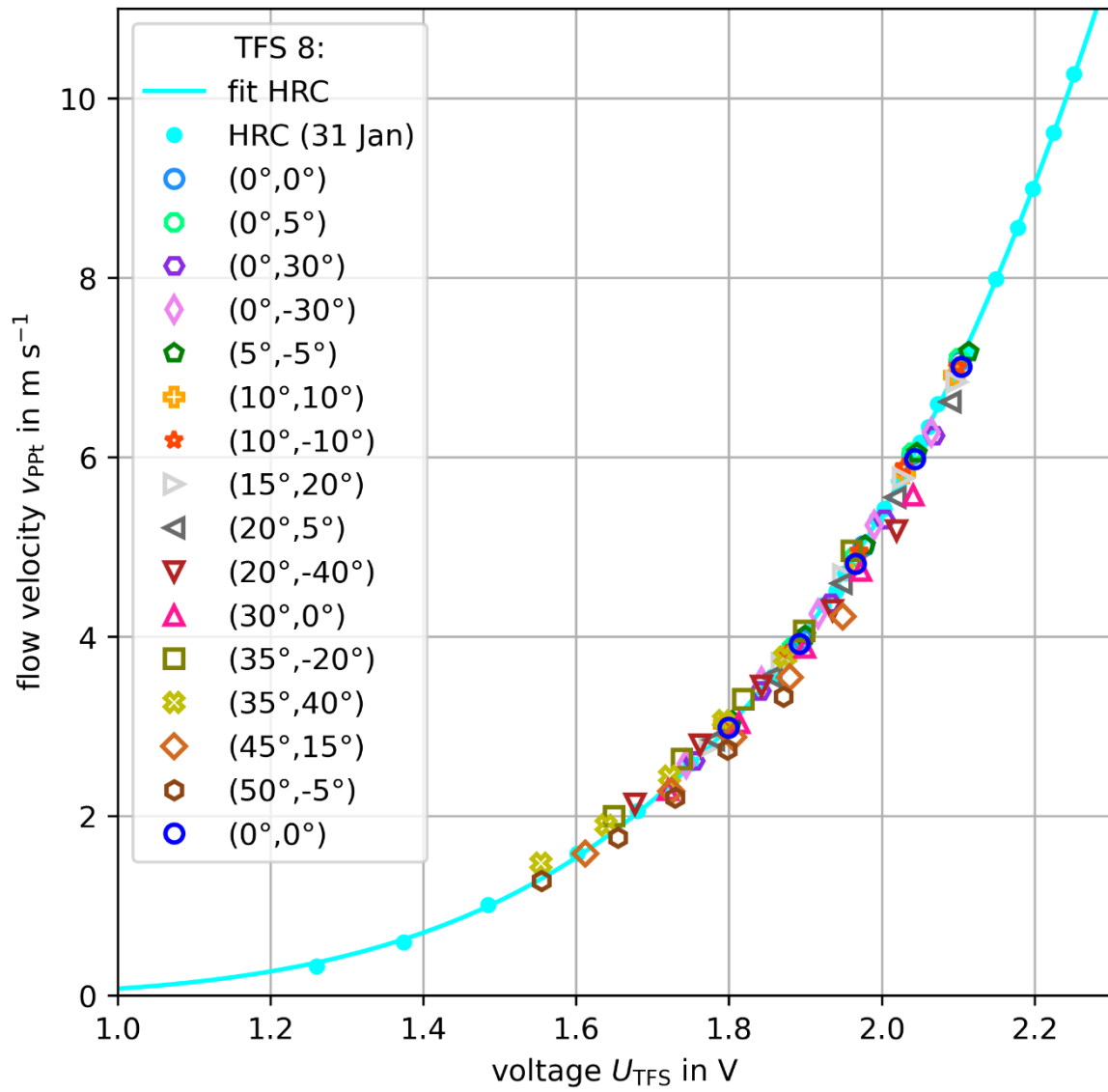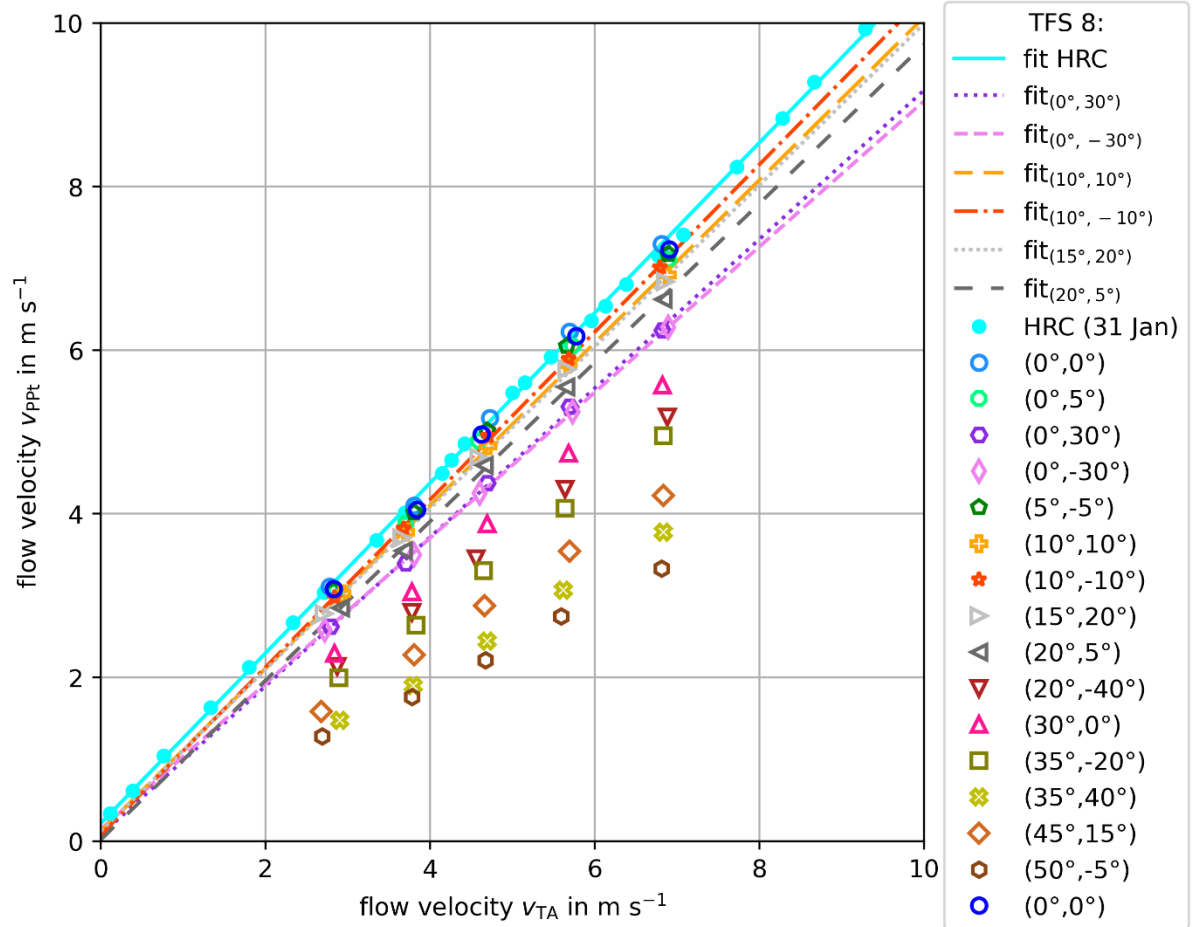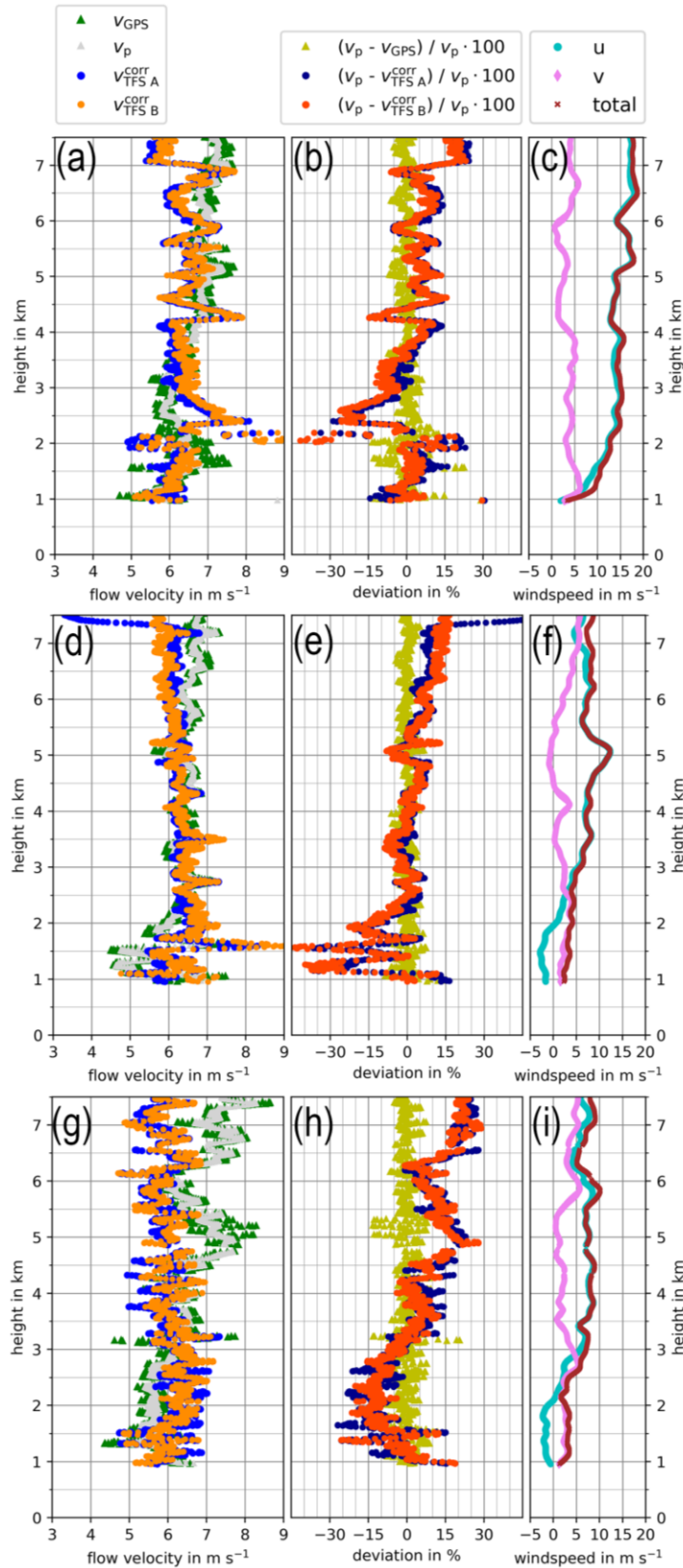
Figure 7

 Tables

Exp. #	PPt	TFS/housing	description
1	yes	no/no	PPt in UCASS housing at position of detection region
2	yes	no/no	"—"
3	yes	yes/yes	PPt at detection region + attached TFS inside its housing
4	yes	yes/yes	"—"
5	yes	no/yes	PPt at TFS position inside TFS housing

Table 1

List of experiments (Exp.) conducted with the PPt at various positions inside the UCASS and TFS housing during wind tunnel flow calibrations.

fit	a	b
(0°,0°) HRC	1.040	0.216
(10°,10°)	0.995	0.119
(10°, -10°)	1.024	0.075
(15°,20°)	0.987	0.120
(20°,5°)	0.972	0.017
(0°, 30°)	0.910	0.073
(0°, -30°)	0.890	0.142

Table 2

Parameters of the linear fit function ($v_{PPt} = a \cdot v_{TA} + b$) to selected UCASS-internal flow velocities measured under variable angle of attack (AOA) in reference to the main wind tunnel flow speed.

angle (φ, ϑ)	deviation $\Delta v_{\text{rel}}^{\text{max}}$ in %	deviation $\Delta \bar{v}_{\text{rel}}$ in %
(0°,0°)	1.1	0.6
(0°,5°)	1.7	1.0
(0°,30°)	3.5	1.8
(0°, -30°)	2.6	1.5
(5°, -5°)	1.5	1.0
(10°,10°)	2.8	0.9
(10°, -10°)	1.6	0.7
(15°,20°)	2.1	0.7
(20°,5°)	3.3	1.5
(20°, -40°)	8.6	4.9
(30°,0°)	7.3	4.1
(35°, -20°)	9.0	4.6
(35°,40°)	13.4	6.1
(45°,15°)	9.5	5.5
(50°, -5°)	10.6	6.7
(0°,0°)	1.4	1.0

Table 3

Maximum ($\Delta v_{\text{rel}}^{\text{max}}$) and mean values ($\Delta \bar{v}_{\text{rel}}$) of the percentual relative deviation of measured flow velocities under variable angle of attack (AOA) for the calibration curve of TFS 8 (cf. Fig. 5).

	deviation $\Delta v_{\text{rel}}^{\text{max}}$ in %	deviation $\Delta \bar{v}_{\text{rel}}$ in %
angle (φ, ϑ)		
(0°, 0°)	1.8	0.8
(0°, 5°)	4.6	3.3
(0°, 30°)	16.5	15.0
(0°, -30°)	16.1	15.3
(5°, -5°)	3.9	2.5
(10°, 10°)	7.3	6.2
(10°, -10°)	6.0	4.5
(15°, 20°)	8.4	7.0
(20°, 5°)	12.3	10.5
(20°, -40°)	33.4	31.1
(30°, 0°)	27.7	24.9
(35°, -20°)	38.1	35.1
(35°, 40°)	54.5	51.8
(45°, 15°)	47.2	44.1
(50°, -5°)	57.5	56.1
(0°, 0°)	3.8	2.1

Table 4

Maximum ($\Delta v_{\text{rel}}^{\text{max}}$) and mean relative deviation ($\Delta \bar{v}_{\text{rel}}$) of in-UCASS measured flow velocity versus the wind tunnel flow speed as a function of the UCASS's angle of attack (AOA) in reference to velocity ratio in zero-position (in correspondence to measurements shown in Fig. 6).

		275 ± 0.3 K	264 ± 0.3 K	254 ± 0.3 K
T_{amb} and corresponding heights in soundings	h (Fig. 7a)	~3930-3990 m	~5700-5790 m	~7250-7310 m
	h (Fig. 7d)	~3690-3740 m	~5490-5560 m	~7250-7320 m
	h (Fig. 7g)	~3700-3770 m	~5400-5490 m	~7230-7300 m
RS41 SGP	Δp		± 1.0 hPa	
	ΔT	—	± 0.3 K	—
	Δh		± 10.0 gpm	
TFS	$v_{\mathrm{TFS}}^{\mathrm{corr}}$ (Fig. 7a)	6.1 – 6.3 m s^{-1}	6.7 – 6.9 m s^{-1}	5.9 – 6.0 m s^{-1}
	$v_{\mathrm{TFS}}^{\mathrm{corr}}$ (Fig. 7d)	6.3 – 6.4 m s^{-1}	6.1 – 6.3 m s^{-1}	5.8 m s^{-1}
	$v_{\mathrm{TFS}}^{\mathrm{corr}}$ (Fig. 7g)	5.0 – 5.5 m s^{-1}	6.3 – 6.4 m s^{-1}	5.4 – 5.7 m s^{-1}
	Δv_{TFS}	± 0.4 %	± 0.4 %	± 0.4 %
	$\Delta v_{\mathrm{TFS}}^{\mathrm{corr}}$	**± 7.9 %**	**± 8.8 %**	**± 6.9 %**
GPS	v_{GPS} (Fig. 7a)	6.7 m s^{-1}	6.7 m s^{-1}	7.6 m s^{-1}
	Δv_{GPS}	**-8.8 – -6.0 %**	**| 0.0 – 3.5 % |**	**-29.3 – -27.7 %**
	v_{GPS} (Fig. 7d)	6.6 m s^{-1}	6.4 m s^{-1}	6.5 m s^{-1}
	Δv_{GPS}	**| -4.4 – -2.9 % |**	**| -4.5 – -1.4 % |**	**-14.2 – -12.5 %**
	v_{GPS} (Fig. 7g)	5.7 m s^{-1}	7.1 m s^{-1}	7.0 m s^{-1}
	Δv_{GPS}	**-14.1 – -4.2 %**	**-12.8 – -10.8 %**	**-30.8 – -23.2 %**

Table 5

Summarised uncertainties 1) ΔT, Δp, and Δh (GPS-altitude) from RS41 SGP radiosondes, 2) the overall uncertainty $\Delta v_{\mathrm{TFS}}^{\mathrm{corr}}$ that result from Gaussian error propagation (Eq. 1 and Eq. 2) and that combine uncertainties from the RS41 SGP data and conditions during TFS calibrations (considering only ΔT, Δp, ΔT_0, and Δp_0) yielding Δv_{TFS} and b) the uncertainty (σ) in v_{TFS} obtained from cold chamber experiments (electronic supplement, Sect. S 1). 3) For three selected ambient temperature conditions (T_{amb} of 275 K, 264 K, and 254 K, from cold chamber experiments) the resulting deviations (Δv_{GPS}) of absolute v_{GPS} in reference to absolute $v_{\mathrm{TFS}}^{\mathrm{corr}}$ from three vertical soundings (see Fig. 7 and adjacent text) are provided for comparison.

References

B+B-Thermo-Technik: Flow sensor element, FLW-122, data sheet, 0141 0316-88, https://shop.bb-sensors.com/out/media/Datasheet_Flow_sensor_FLW-122_new.pdf (called 02 Sep. 2024), Donaueschingen, 2016, 2016.

Bearman, P. W.: Corrections for the effect of ambient temperature drift on hot-wire measurements in incompressible flow DISA Info, Bull, 11, 25-30, 1971.

Bezantakos, S., Costi, M., Barmpounis, K., Antoniou, P., Vouterakos, P., Keleshis, C., Sciare, J., and Biskos, G.: Qualification of the Alphasense optical particle counter for inline air quality monitoring, Aerosol Sci Tech, 55, 361-370, https://doi.org/10.1080/02786826.2020.1864276, 2020.

Cardell, G.: A Note on the Temperature-Dependent Hot-Wire Calibration Method of Cimbala and Park, Exp Fluids, 14, 283-285, 1993.

Cimbala, J. M. and Park, W. J.: A Direct Hot-Wire Calibration Technique to Account for Ambient-Temperature Drift in Incompressible-Flow, Exp Fluids, 8, 299-300, https://doi.org/10.1007/BF00187234, 1990.

Dirksen, R. J., Bodeker, G. E., Thorne, P. W., Merlone, A., Reale, T., Wang, J., Hurst, D. F., Demoz, B. B., Gardiner, T. D., Ingleby, B., Sommer, M., von Rohden, C., and Leblanc, T.: Managing the transition from Vaisala RS92 to RS41 radiosondes within the Global Climate Observing System Reference Upper-Air Network (GRUAN): a progress report, Geosci. Instrum. Method. Data Syst., 9, 337-355, https://doi.org/10.5194/gi-9-337-2020, 2020.

EUFAR: European Facility for Airborne Research, https://www.eufar.net/aircrafts/list-matrix (called 04 Dec. 2024), 2000.

Girdwood, J.: Optical Measurement of Airborne Particles on Unmanned Aircraft, Ph.D. thesis, University of Hertfordshire, Hatfield, UK, https://doi.org/10.18745/th.27277, 2023.

Girdwood, J., Stanley, W., Stopford, C., and Brus, D.: Simulation and field campaign evaluation of an optical particle counter on a fixed-wing UAV, Atmos Meas Tech, 15, 2061-2076, https://doi.org/10.5194/amt-15-2061-2022, 2022.

Golden, J. H., Serafin, R., Lally, V., and Facundo, J.: Atmospheric Sounding Systems, in: Mesoscale Meteorology and Forecasting, edited by: Ray, P. S., American Meteorological Society, Boston, MA, 50-70, https://doi.org/10.1007/978-1-935704-20-1_4, 1986.

Guellouz, M. S. and Tavoularis, S.: A Simple Pendulum Technique for the Calibration of Hot-Wire Anemometers over Low-Velocity Ranges, Exp Fluids, 18, 199-203, https://doi.org/10.1007/BF00230265, 1995.

IPCC: International Panel on Climate Change; AR6 synthesis report: Climate change 2023 (No. AR6), United Nations https://www.ipcc.ch/report/ar6/syr/, 2023.

Kandler, K., Benker, N., Bundke, U., Cuevas, E., Ebert, M., Knippertz, P., Rodriguez, S., Schütz, L., and Weinbruch, S.: Chemical composition and complex refractive index of Saharan Mineral Dust at Izana, Tenerife (Spain) derived by electron microscopy, Atmos Environ, 41, 8058-8074, https://doi.org/10.1016/j.atmosenv.2007.06.047, 2007.

Kasai, T., Tsuchiya, M., Takami, K., Hayashi, M., and Iwasaka, Y.: Balloon borne optical particle counter for stratospheric observation, Rev Sci Instrum, 74, 1082-1092, https://doi.org/10.1063/1.1533791, 2003.

Kezoudi, M., Tesche, M., Smith, H., Tsekeri, A., Baars, H., Dollner, M., Estellés, V., Bühl, J., Weinzierl, B., Ulanowski, Z., Müller, D., and Amiridis, V.: Measurement report: Balloon-borne in situ profiling of Saharan dust over Cyprus with the UCASS optical particle counter, Atmos Chem Phys, 21, 6781-6797, https://doi.org/10.5194/acp-21-6781-2021, 2021.

Matsumura, T., Hayashi, M., Fujiwara, M., Matsunaga, K., Yasui, M., Saraspriya, S., Manik, T., and Suripto, A.: Observations of Stratospheric Aerosols by Balloon-borne Optical Particle Counter at Bandung, Indonesia, Journal of the Meteorological Society of Japan. Ser. II, 79, 709-718, https://doi.org/10.2151/jmsj.79.709, 2001.

Schön, M., Savvakis, V., Kezoudi, M., Platis, A., and Bange, J.: OPC-Pod: A New Sensor Payload to Measure Aerosol Particles for Small Uncrewed Aircraft Systems, Journal of Atmospheric and Oceanic Technology, 41, 499-513, https://doi.org/10.1175/JTECH-D-23-0078.1, 2024.

994 The SciPy community. scipy.optimize.curve_fit:
995 https://docs.scipy.org/doc/scipy/reference/generated/scipy.optimize.curve_fit.html, last
996 access: 21. April 2023.

998 Smit, H. G. J., Poyraz, D., Van Malderen, R., Thompson, A. M., Tarasick, D. W., Stauffer, R. M., Johnson,
999 B. J., and Kollonige, D. E.: New insights from the Jülich Ozone Sonde Intercomparison Experiment:
1000 calibration functions traceable to one ozone reference instrument, Atmos. Meas. Tech., 17, 73-112,
1001 https://doi.org/10.5194/amt-17-73-2024, 2024.

1003 Smith, H. R., Ulanowski, Z., Kaye, P. H., Hirst, E., Stanley, W., Kaye, R., Wieser, A., Stopford, C.,
1004 Kezoudi, M., Girdwood, J., Greenaway, R., and Mackenzie, R.: The Universal Cloud and Aerosol
1005 Sounding System (UCASS): a low-cost miniature optical particle counter for use in dropsonde or
1006 balloon-borne sounding systems, Atmos Meas Tech, 12, 6579-6599,
1007 https://doi.org/10.5194/amt-12-6579-2019, 2019.

1009 Snels, M., Cairo, F., Di Liberto, L., Scoccione, A., Bracaglia, M., and Deshler, T.: Comparison of
1010 Coincident Optical Particle Counter and Lidar Measurements of Polar Stratospheric Clouds Above
1011 McMurdo (77.85°S, 166.67°E) From 1994 to 1999, Journal of Geophysical Research: Atmospheres,
1012 126, e2020JD033572, https://doi.org/10.1029/2020JD033572, 2021.

1014 Sonntag, D.: Advancements in the field of hygrometry, Meteorol Z, 3(2),
1015 https://www.osti.gov/etdeweb/biblio/6907980, 1994.

1017 Stier, P., van den Heever, S. C., Christensen, M. W., Gryspeerdt, E., Dagan, G., Saleeby, S. M., Bollasina,
1018 M., Donner, L., Emanuel, K., Ekman, A. M. L., Feingold, G., Field, P., Forster, P., Haywood, J., Kahn, R.,
1019 Koren, I., Kummerow, C., L'Ecuyer, T., Lohmann, U., Ming, Y., Myhre, G., Quaas, J., Rosenfeld, D.,
1020 Samset, B., Seifert, A., Stephens, G., and Tao, W.-K.: Multifaceted aerosol effects on precipitation,
1021 Nat Geosci, 17, 719-732, https://doi.org/10.1038/s41561-024-01482-6, 2024.

1023 Vaisala: Radiosonde RS41-SGP, datasheet; https://docs.vaisala.com/v/u/B211444EN-J/en-US,
1024 2024.

1026 Vömel, H. and Fujiwara, M.: Aerological Measurements, in: Springer Handbook of Atmospheric
1027 Measurements, edited by: Foken, T., Springer International Publishing, Cham, 1247-1280,
1028 https://doi.org/10.1007/978-3-030-52171-4_46, 2021.

1030 Vömel, H. and Ingleby, B.: Chapter 2 - Balloon-borne radiosondes, in: Field Measurements for
1031 Passive Environmental Remote Sensing, edited by: Nalli, N. R., Elsevier, 23-35,
1032 https://doi.org/10.1016/B978-0-12-823953-7.00010-1, 2023.
1033